J Appl Electrochem (2007) 37:1245–1259
DOI 10.1007/s10800-007-9414-1

ORIGINAL PAPER

Modelling and experimental validation of a high temperature polymer electrolyte fuel cell

K. Scott · S. Pilditch · M. Mamlouk

Received: 6 December 2006 / Revised: 31 August 2007 / Accepted: 1 September 2007 / Published online: 22 September 2007

Abstract A steady-state, isothermal, one dimensional model of a proton exchange membrane fuel cell (PEMFC), with a polybenzimidazole (PBI) membrane, was developed. The electrode kinetics were represented by the Butler–Volmer equation, mass transport was described by the multi-component Stefan–Maxwell equations and Darcy's law and the ionic and electronic resistances described by Ohm's law. The model incorporated the effects of temperature and pressure on the open circuit potential, the exchange current density and diffusion coefficients, together with the effect of water transport across the membrane on the conductivity of the PBI membrane. The polarisation curves predicted by the model were validated against experimental data for a PEMFC operating in the temperature range of 125–200 °C. There was good agreement between experimental and model data of the effect of temperature and oxygen/air pressure on cell performance. The model was used to simulate the effect of catalyst loading and the Pt/carbon ratio on cell performance and, in the latter case, a 40 wt.% Pt/C ratio gave the highest peak power density.

Keywords Polymer electrolyte fuel cell · Polybenzimidazole · PBI · Membrane · Modelling

Notations

A_{act}	Active area of catalyst particles (m^2)
A_D	Anode diffusion region (No units)
A_M	Anode microporous region (No units)
A_R	Anode reaction region (No units)
A_F	Anode flow region (No units)
a	Height of catalyst (m)
b	Width of catalyst (m)
c_i	Molar density/concentration of component i (mol m^{-3})
C_D	Cathode diffusion region (No units)
C_R	Cathode reaction/catalyst region (No units)
c	Depth of catalyst (No units)
D_{ij}	Stefan–Maxwell diffusivities (m^2 s^{-1})
D_{ij}^{eff}	Effective Stefan–Maxwell diffusivities (m^2 s^{-1})
$\tilde{D}_{ij}$	Symmetric diffusivities (m^2 s^{-1})
E	Potential (V)
E_0^0	Standard state reference potential (V)
F	Faraday constant (A s mol^{-1})
G	Gibbs free energy (J mol^{-1})
H	Enthalpy (J mol^{-1})
I	Cell current density (A m^{-2})
j_e	Electronic current (A m^{-2})
j_i	Ionic/proton current (A m^{-2})
j_o	Exchange current density (A m^{-2})
j_{o_β}	Exchange current density at electrode β (A m^{-2})
j_{o_a}	Exchange current density in anode (A m^{-2})
j_V^β	Current density source term in cathode (A m^{-3})
j_V^a	Current density source term in anode (A m^{-3})
j_V^c	Current density source term in cathode (A m^{-3})
J_i	Diffusion flux (kg m^{-2} s^{-1})
k	Permeability of the porous media (m^2)
L	Catalyst loading (g m^{-2})
M	Membrane region (No units)
M_{cat}	Mass of the catalyst (g)
M_i	Mass of species i (kg mol^{-1})
n	Number of electrons (No units)
N_i	Total flux of species i (kg m^{-2} s^{-1})
p	Total pressure (m^{-1} kg s^{-2})

K. Scott (✉) · S. Pilditch · M. Mamlouk
School of Chemical Engineering and Advanced Materials, University of Newcastle upon Tyne, Merz Court, The University, Newcastle-upon-Tyne NE1 7RU, UK
e-mail: k.scott@newcastle.ac.uk

p_i Partial pressure of species i (bar)
Q Constant in Stefan–Maxell diffusion (No units)
u Velocity vector (m s^{-1})
R Gas constant (J K^{-1} mol^{-1})
$\bar{R}$ Source terms (kg m^{-3} s^{-1})
R_P Surface area of platinum (m^2 g^{-1})
S_A Ratio of real catalyst and (m^2 m^{-3}), geometric volumes (m^{-1})
S Entropy (J mol^{-1} K^{-1})
S^o Entropy at standard reference temperature (J mol^{-1} K^{-1})
T Temperature (K)
U_{cell} Cell potential (V)
v_i Molecular diffusion volumes of species i (m^2)
V_n Volume of composition n
x_i Mole fraction of species i (No units)
w_i Mass fraction of species i (No units)

Greek

ε Porosity fraction (No units)
α_a Anode transfer coefficient at the relevant electrode (No units)
α_c Cathode transfer coefficient at the relevant electrode (No units)
γ_i Kinetic exponent of the species i in the Butler–Volmer equation (No units)
κ Ionic conductivity (S m^{-1})
μ_β Pore-fluid viscosity in electrode β (m^{-1} kg s^{-1})
ρ Density (kg m^{-3})
σ Electronic conductivity (S m^{-1})
ϕ Electric potential of protons (V)
ϕ_s Electric potential of the electrons (V)
η Overpotential (V)
β Electrode (anode or cathode) (No units)

Superscripts and subscripts

A Area
a Anode
act Activation region
an Anodic
β Electrode (anode or cathode)
c Cathode
cb Carbon
cat Catalyst
ct Cathodic
D Diffusion region
eff Effective in that region
F Flow channel
h_2 Hydrogen
i Ion phase or species i
ox Oxidation
M Microporous region
n Composition n
pbi PBI membrane
pt Platinum
s Solid phase (electrons)
R Reaction/catalyst
red Reduction
v Volume
0 Reference state

1 Introduction

Proton exchange membrane fuel cells (PEMFCs) are being developed as alternatives to internal combustion engines, because of their high power density, high energy conversion efficiency and low emission levels. However, one of the major issues limiting the introduction of PEMFCs for several applications is poisoning of platinum-based anode catalysts by trace amounts of CO, inevitably present in the reformed fuel. In order to alleviate this problem and improve the power density of the cell, operation at temperatures above 100 °C is preferred [1–4]. In addition, the higher temperatures will enable more effective cooling of the cell stacks and provide a means for combined electrical energy and heat generation.

Nafion®-type perfluorosulfonated polymers have been used in PEMFCs at temperatures between 20 and 80 °C. The proton conductivity of the Nafion® membrane is closely linked to the level of hydration. Therefore, water management is complicated and needs to be closely controlled. The conductivity of Nafion® polymers, at temperature >80 °C, is too low for fuel cell operation at atmospheric pressure because they dehydrate under these conditions [5].

In recent years, several research groups have been developing new membranes [6–9], based on polybenzimidazoles; the most widely used acid-doped polymer is poly[2,2-(*m*-phenylene)-5,5 bibenzimidazole], generically referred to as polybenzimidazole (PBI). PBI fuel cells operate in the temperature range of 120–200 °C. The higher operating temperature limits the effect of CO poisoning of the platinum catalyst. Therefore, using hydrogen, produced from reforming of natural gas, oil or coal, that contains relatively large concentrations of CO, is more viable at higher temperatures of operation associated with PBI fuel cells.

PBI membranes, when doped with phosphoric acid, do not rely on hydration for conductivity; a significantly lower water content of the membrane, compared to Nafion, is required for proton transport. Therefore, water management does not need to be so closely controlled. Also, as the cell is operated at a higher temperature, the water can be considered to be in the vapour phase and the problems of

liquid water blocking the catalyst pores and two phase flow between gas and liquid are alleviated. To obtain sufficient ionic conductivity, the PBI membrane must be impregnated with orthophoshoric acid. The presence of phosphoric acid in PBI, which is used as an ionic conductor in the electrocatalyst layers, will influence the electrode kinetics. Thus, two issues associated with phosphoric acid in the PBI based fuel cell are the lower activity of the electrocatalysts and the potential loss of the acid into the fuel cell gas/vapour exhaust streams.

There are numerous mathematical models of Nafion® type PEMFCs that have been reported in the literature. The first phenomenological model of a PEMFC with a Nafion® membrane was by Bernardi and Verbrugge [10]; since then, significant developments have been made. For example, three dimensional models have been reported by Mazumder [11, 12], and by Hu and Berning [13, 14]. Noponen et al. [15–17] used finite element software to model concentration and current distributions [15] and to map liquid saturation and temperature distributions [16, 17] for comparison with experimental data. Commercial finite element software has also been used by Guevelioglu [18] to solve equations describing multi-component flow in diffusion layers and flow channels. Models of mass transport in fuel cells have also been reported by Scott [19].

In comparison, there has been little modelling of PEMFCs with PBI membranes. One recent paper [20] reported modelling of current distribution, but ignored those in the electrocatalyst layers and assumed the high field (Tafel) approximation to describe electrode kinetics. A second recent publication [21] reported modelling of the variations in cell temperature that occur in high temperature PEMFCs.

Modelling of PBI PEMFCs will increase understanding of their behaviour, enable prediction of their performance and assist with their operational control. Thus, a one dimensional (1D) model of the high temperature PBI based PEMFC is described in this paper that includes the potential and current distributions in the catalyst layers and considers multi-component mass transport through diffusion and catalysts layers.

2 Experimental

The membrane electrode assembly used in the experiments consisted of a phosphoric acid doped polybenzimidazole membrane, onto which anode and cathode catalyst layers were bonded. The catalyst layers were covered by gas diffusion layers, consisting of a micro-porous layer of PTFE bonded Ketjen Black 300 carbon (Azko Nobel, UK) covered by a hydrophobic carbon paper (Toray, with PTFE). The catalyst layers consisted of a mixture of carbon (Vulcan) supported Pt with PBI and phosphoric acid.

The fabrication of the membrane-electrode-assemblies (MEAs) was achieved as follows. A micro-porous layer was deposited by air-brushing an ink, composed of 1 mg cm^{-2} Ketjen Black 300 carbon and Teflon (40 wt.%) as binder in isopropanol, onto a carbon paper support layer (Toray graphite paper, TGPH-090, 20% wet-proofed, E-Tek Inc.). The function of the microporous carbon layer was to avoid the penetration of catalyst particles into the carbon paper during hot pressing.

The catalyst inks were prepared with Pt/C powder (20% Pt on Vulcan XC-72, Etek Inc.), polybenzimidazole (PBI) solution (5 wt.% in *N*,*N*-dimethylacetamide (DMAc)) and either DMAc or acetone as solvent. DMAc was used for the so-called solution method, as PBI is soluble in DMAc and acetone was used for the colloidal method (PBI forms a colloid with a mixture of acetone and DMAc). The loadings of platinum catalyst and polymer were both 0.5 mg cm^{-2}. The inks were spayed by air-brushing onto the micro-porous layer. After air-brushing, the electrodes were dried and sintered at 190 °C for an hour and then doped with 2.0 M phosphoric acid and left to equilibriate overnight. Membrane electrode assemblies were made by hot pressing the electrodes and the acid doped membranes (stored in 11.0 M phosphoric acid for more than 2 weeks) at 150 °C and 0.1 ton cm^{-2} pressure for 10 min.

Figure 1 shows SEM micrographs of the two catalyst layer surfaces. The electrode prepared by the "solution method" had a more uniform and dense structure compared with the electrode made by the colloidal method (A). The size of agglomerates was larger for the "colloidal" electrode. The electrode made by the solution method (B) had a smaller secondary pore volume; as measured by mercury porosimetry [22], which could impede mass transport, as evident from cell polarization curves at higher current densities (see Fig. 6).

To perform cell tests, the MEA was in contact with high-density graphite blocks, impregnated with phenolic resin, into which parallel gas parallel flow channels were machined. The ridges between the channels provided electrical contact to the carbon electrodes and the total machined cross sectional area, of 9 cm^2, was taken as the active cell area. Electric cartridge heaters were mounted at the rear of the graphite blocks to maintain the desired cell temperature, which was monitored by thermocouples embedded in the graphite blocks and controlled with a temperature controller. Gold-plated steel bolts were screwed into the blocks to allow electrical contact. Hydrogen and air were fed to the cell at flow rates of 0.2 and 0.45 dm^3 min^{-1}, respectively. These flow rates were in excess of stoichiometric requirements for the electrode reactions ($\lambda = 1.2$ H_2/O_2 and $\lambda = 2.2$ air).

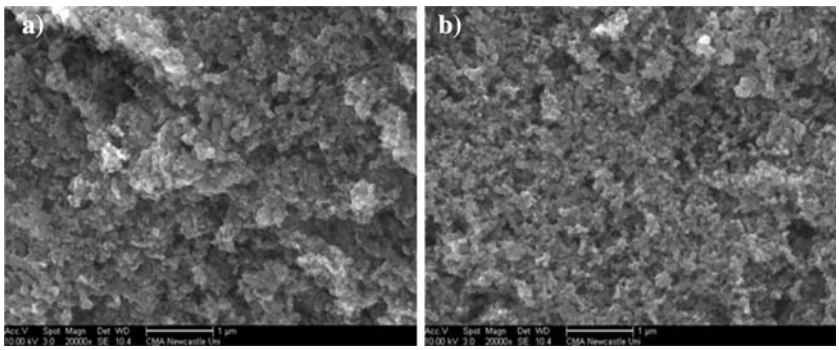

Fig. 1 Scanning electron micrographs of the electrode catalyst surfaces (**a**) colloidal electrode—A, (**b**) solution electrode—B

2.1 Polymer synthesis

Vogel and Marvel [23] were the first to prepare poly[2,2-*m*-(phenylene)-5,5-bibenzimidazole from 3,3-diaminobenzidine and isophthalic acid in polyphosphoric acid (PPA) by solution polycondensation at temperatures between 170 and 200 °C, according to the reaction below:

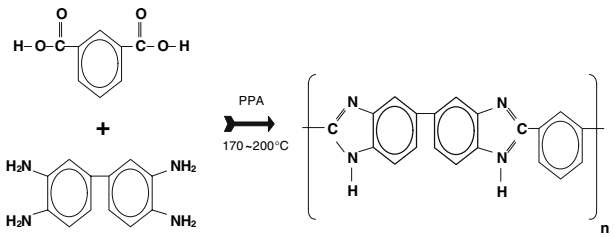

The PBI obtained had an inherent viscosity (IV) of 0.6–0.8 dl g^{-1} when measured as a concentration of 0.4 g of PBI in 100 cm^3 of 97% sulphuric acid at 25 °C. This IV corresponds to a weight average molar mass of 100–180 kDa. Higher molecular weights have been achieved by the addition of an aryl-halo phosphorus catalyst, such as triphenyl phosphite or dichlorophenylphosphine. For example, using 1 wt.% of catalyst increased the molecular weight of the polymer from 400 to 600 kDa [24]. The Vogel and Marvel method of PBI synthesis [23] was used in this work.

In the synthesis of PBI, the catalyst not only increased the molecular weight, but also broadened its polydispersity. Two samples from the same PBI batch (using triphenylphosphite as catalyst) were dissolved in DMAc, one at room temperature and the other at 250 °C, and their molecular weight distributions were determined. The sample dissolved at room temperature was 100% soluble, while the sample dissolved at 250 °C required filtration to remove approximately 10 wt.% of a non-soluble part. The resulting molecular weight distributions are given in Table 1 and compared with those of a commercially available PBI and a PBI synthesised without catalyst. PBI synthesised using catalyst had a much higher molecular weight. The polymer obtained after dissolving in DMAc at low temperature had higher molecular weight than that dissolved at 250 °C. The observed reduction in the average molecular weight and the narrowed polydispersity, after heat treatment, can be attributed to cross-linking that occurred during heat treatment with DMAc, where 10 wt.% of the polymer become non-soluble.

Table 1 Effect of catalyst on PBI molecular weight and polydispersity

Sample	M_w	M_n	M_w/M_n
Commercial (dissolved) liquid form (Aldrich)	170,000	65,700	2.6
	171,000	65,400	2.6
Synthesised without catalyst	186,000	66,500	2.8
	179,000	63,000	2.8
Synthesised with catalyst dissolved at 250 °C	415,000	88,100	4.7
	412,000	91,900	4.5
Commercial powder form (Aldrich)	158,000	57,300	2.6
	154,000	58,300	2.6
Synthesised with catalyst dissolved at room temperature	623,000	116,000	5.4
	609,000	112,000	5.4

$M_w = \frac{\sum_i N_i M_i^2}{\sum_i N_i M_i}$ is the weight average molecular weight and $M_n = \frac{\sum_i N_i M_i}{\sum_i N_i}$ is the number average molecular weight. N_i is the number of molecules of molecular weight M_i

2.2 Membrane preparation

PBI powder (IV = 0.7 dl g^{-1}) was dissolved in *N*,*N*-dimethylacetamide (DMAc) at a temperature of 250 °C (80 °C above the boiling point of DMAc) in an autoclave. In this procedure, the autoclave was purged with nitrogen and heated gradually to 250 °C, while the pressure increased to 6 bar. The temperature was then held for 5 h with the solution stirred to allow the majority of the polymer to dissolve. Lithium chloride (2 wt.%) was added to the

solution in order to prevent the 'phasing out' phenomenon [25]. The cooled solution was then filtered to remove the un-dissolved polymer. The solution was then poured onto an optical glass and kept in an oven at a temperature of 90–110 °C for 12 h to produce a 40 μm thick membrane. After cutting the membrane into several samples, the solvent and residual traces of lithium chloride were removed by boiling in de-ionised water for 1 h.

For fuel cell tests and characterisation, the membranes were doped with phosphoric acid. Doping was achieved by immersing the membranes in a phosphoric solution of known concentration for a minimum period of 4 days at room temperature. After doping, the membranes were dried under vacuum at 110 °C until a constant weight was achieved [26]. The doping level was calculated from the membrane weight gain before and after doping [7]. The effects of doping level on membrane tensile stress and proton conductivity were studied; it was found that for PBI membranes with medium molecular weights, i.e. IV between 0.6 and 0.9 dL g^{-1}, the optimum doping level was around 5 mol H_3PO_4 per PBI repeat unit. Therefore, increasing the doping level increased the membrane proton conductivity; but significantly reduced its mechanical strength.

2.3 Conductivity measurements

To assess the acid doped PBI membranes for high temperature PEMFC, their conductivities were measured using the four point probe or Kelvin probe technique, by frequency response analysis (Voltech TF2000, UK). The technique involved four equally spaced probes in contact with the measured material; two of the probes were used to source current while the other two were used to measure the voltage drop. The membranes were cut into 10×50 mm strips and placed across four platinum foils with equal spacing of 5 mm. AC impedance measurements were carried out between frequencies of 1 and 20 kHz. The membranes were held at the desired conditions of temperature and humidity for 3 h to ensure steady state was achieved and measurements were taken at 30 min intervals.

The effect of relative humidity (RH) on membrane conductivity was investigated in a test rig which incorporated a humidifier, that could supply a water saturated nitrogen stream to a membrane conductivity test cell, and a humidity analyser. For measurements, the membrane was maintained at the desired temperature in the test cell and the relative humidity was changed by varying the humidifier temperature, whilst maintaining the nitrogen flow rate at 1.5 dm^3 min^{-1}. Relative humidity was measured using a Vaisala HUMICAP® intrinsically safe humidity and temperature transmitter.

PBI conductivity strongly depends on three main factors: acid doping level, temperature and relative humidity. During conductivity measurements, the doping level was fixed at 5.6 mol of H_3PO_4 per PBI repeat unit, whilst the temperature and the relative humidity were varied. The values of conductivities obtained are shown in Fig. 2. Conductivity increased with an increase in humidity and temperature. However, at a similar relative humidity, no significant gain in proton conductivity was obtained by increasing the temperature above 175 °C. This effect was probably a result of water lost by phosphoric acid dimerisation. It is known that, at elevated temperatures, phosphoric acid starts to dehydrate; which can occur in many stages, the first two of which are shown below:

$$\text{First stage: } 2H_3PO_4 \leftrightarrow H_4P_2O_7 + H_2O \uparrow$$
$$\text{Second stage: } H_4P_2O_7 + H_3PO_4 \leftrightarrow H_5P_3O_{10} + H_2O \uparrow$$

The equilibrium concentrations of these reversible reactions depend on temperature and relative humidity and the dimerised products have lower proton conductivity than phosphoric acid [27].

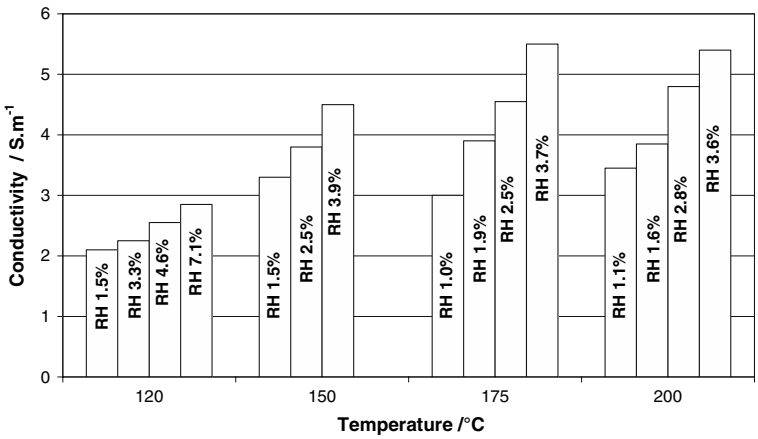

Fig. 2 Effects of temperature and relative humidity on conductivities of the PBI membrane

3 Mathematical model of the fuel cell

The mathematical model of the fuel cell was one dimensional and considered the fuel cell to consist of two diffusion layers, anode and cathode catalyst layers and the membrane, as shown in Fig. 3. The reactions in the cell were:

$$\text{Anode} \quad 2H_2 \Rightarrow 4H^+ + 4e^- \tag{1}$$

$$\text{Cathode} \quad O_2 + 4H^+ + 4e^- \Rightarrow 2H_2O \tag{2}$$

The assumptions adopted in the model were:

- Steady state and isothermal operation
- Ideal gas behaviour
- Single phase behaviour
- Membrane was impermeable to hydrogen and oxygen
- Negligible contact resistances between components
- No membrane swelling

Isothermal operation was a reasonable assumption as the test cell temperature was controlled using electrical heating. Ideal gas behaviour was appropriate, as the cell was not operated at high pressure. As the cell was operated at relatively high temperatures, above the normal boiling point of water, it was reasonable to assume there was no liquid saturation and single phase behaviour applied. The flow channel was not included in the model; the boundary conditions between the flow channel and the diffusion layer were taken as the feed gas compositions.

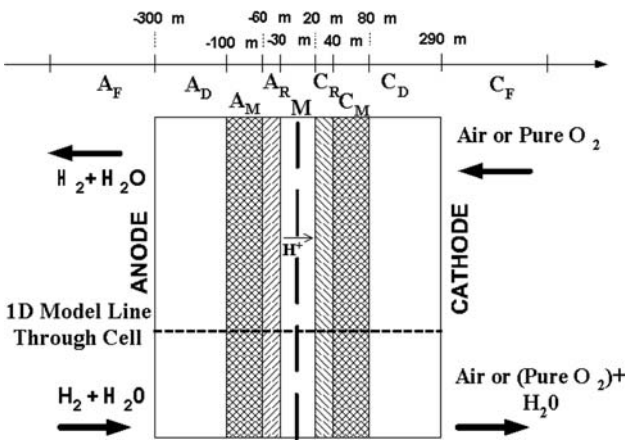

Fig. 3 Schematic diagram of the fuel cell cross section showing anode, cathode and membrane regions. Anode: A_F, Flow channel; A_D, Diffusion layer; A_M, Microporous layer; A_R, Catalyst layer. Membrane: M, Membrane. Cathode: C_F, Flow channel; C_D, Diffusion layer; C_M, Microporous layer; C_R, Catalyst layer

4 Model equations

4.1 Thermodynamics

The Nernst equation for the equilibrium potential (E) can be written, with partial pressure (p) used to approximate the reactant and product activities, as

$$E = E^0 - \frac{RT}{nF}\ln\left[\frac{p_{H_2}(p_{O_2})^{0.5}}{p_{H_2O}}\right] \tag{3}$$

with

$$E^0 = E_0^0 + (T - T_0)\left(\frac{\Delta S^0}{nF}\right) \tag{4}$$

where S is the entropy; T, temperature; F, Faraday's constant and E_0^0 is the standard reference potential (298.15 K and 1 atm); 1.229 V for liquid water and 1.18 V for gaseous water [28].

The thermodynamic values of enthalpy, free energy and entropy for water used in this work were [29]:

water as liquid:

$$\Delta H = -285.830, \quad \Delta G = -237.130\,\text{J mol}^{-1}$$
$$\text{and } \Delta S = -164.25\,\text{J mol}^{-1}\,K^{-1}$$

water as vapour:

$$\Delta H = -241.820, \quad \Delta G = -228,570\,\text{J mol}^{-1}.$$

The entropy was a function of temperature (ignoring pressure effects) given by:

$$\Delta S = f(T) = \frac{-18.449 - 0.01283T}{n}\,\text{J mol}^{-1}\,\text{K}^{-1} \tag{5}$$

For T = 393 K, Eq. 5 gives $\Delta S = -47\,\text{J mol}^{-1}\,\text{K}^{-1}$.

From Eqs. 3, 4 and 5 we obtain

$$E = 1.229 - 0.85\cdot 10^{-3}(T - 298.15) + \frac{RT}{nF}\ln\left[\frac{p_{H_2}(p_{O_2})^{0.5}}{a_{H_2O}}\right] \tag{6}$$

and for gaseous water:

$$E = 1.18 - \frac{\Delta S(T)}{nF}(T - 298.15) + \frac{RT}{nF}\ln\left[\frac{p_{H_2}(p_{O_2})^{0.5}}{p_{H_2O}}\right]. \tag{7}$$

The activity of liquid water was assumed to be 1.0.

The boiling point for water varies with pressure: e.g. 100, 125, 140 °C for pressure of 1, 2 and 3 bar,

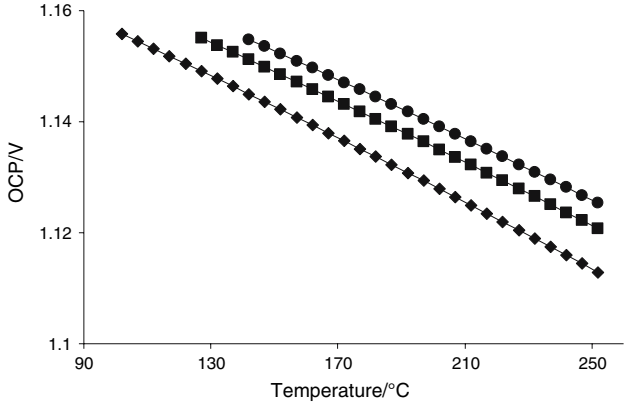

Fig. 4 Effect of temperature on open circuit potential. Case A—partial pressure of oxygen, hydrogen and water vapour 1 bar. Case B—partial pressure of oxygen and hydrogen 2 bar and water vapour 1 bar. Case C—partial pressure of oxygen and hydrogen 3 bar and water vapour 1 bar

respectively [27]. Figure 4 shows the variation of equilibrium potential for vapour phase water, calculated from Eq. 7 at the three different pressures.

4.2 Mass transport

In fuel cells, the fuel (hydrogen) and oxidant (air) flow through channels next to the MEA and pass through porous "gas diffusion" media, before reaching and passing through the porous electrocatalyst layer. In this model, mass transport effects in the flow channel were ignored, as the experimental electrode size was small, and only transport processes in the porous media were considered. The two transport phenomena considered were diffusion and convection.

The total mass flux N_i for species i, due to diffusion and convection, is given by:

$$N_i = J_i + \rho_i u \tag{8}$$

where J_i is the diffusion flux and $\rho_i\, u$ is the convective flux, i.e. the product of density and velocity.

The Stefan–Maxwell equation and Darcy's law were used to model the mass transport processes. In the anode side of the cell, hydrogen and possibly water vapour (with CO_2 if formed during fuel reforming) were considered and in the cathode side there was a mixture of oxygen, nitrogen and water vapour. To account for the effect of interactions between species on mass transport, the Stefan–Maxwell equation was used in the following form:

$$\nabla \cdot \left[\rho u \cdot w_k - \rho w_k \sum_{l=1} \widetilde{D}_{kl} \left\{ \nabla x_l + (x_l - w_l) \frac{\nabla p}{p} \right\} \right] = \bar{R}, \tag{9}$$

where $\widetilde{D}_{kl}$ are the symmetric diffusivities. The first term $\rho u \cdot w_k$ is the convection term. The velocity vector u was calculated from Darcy's law. The second term in the Stefan–Maxwell equation describes the effect of diffusion.

The symmetric diffusivities were calculated from the effective Stefan–Maxwell diffusivities:

$$\widetilde{\mathrm{D}}_{11} = \frac{\dfrac{(w_2+w_3)^2}{x_1 \mathrm{D}_{23}^{eff}} + \dfrac{w_2^2}{x_2 \mathrm{D}_{13}^{eff}} + \dfrac{w_3^2}{x_3 \mathrm{D}_{12}^{eff}}}{\dfrac{x_1}{\mathrm{D}_{12}^{eff}\mathrm{D}_{13}^{eff}} + \dfrac{x_2}{\mathrm{D}_{12}^{eff}\mathrm{D}_{23}^{eff}} + \dfrac{x_3}{\mathrm{D}_{13}^{eff}\mathrm{D}_{23}^{eff}}}$$

$$\widetilde{\mathrm{D}}_{12} = \frac{\dfrac{w_1(w_2+w_3)}{x_1 \mathrm{D}_{23}^{eff}} + \dfrac{w_2(w_1+w_3)}{x_2 \mathrm{D}_{13}^{eff}} + \dfrac{w_3^2}{x_3 \mathrm{D}_{12}^{eff}}}{\dfrac{x_1}{\mathrm{D}_{12}^{eff}\mathrm{D}_{13}^{eff}} + \dfrac{x_2}{\mathrm{D}_{12}^{eff}\mathrm{D}_{23}^{eff}} + \dfrac{x_3}{\mathrm{D}_{13}^{eff}\mathrm{D}_{23}^{eff}}}. \tag{10}$$

Additional entries of the symmetric diffusivities were constructed by permutation of the indices, that is $\widetilde{\mathrm{D}}_{12} = \widetilde{\mathrm{D}}_{21}$.

The Stefan–Maxwell diffusivities D_{ij} are given by an empirical equation based on the kinetic gas theory:

$$\mathrm{D}_{ij} = \mathrm{Q} \frac{T^{1.75}}{p(v_i^{1/3} + v_j^{1/3})^2} \left[\frac{1}{M_i} + \frac{1}{M_j} \right]^{1/2}, \tag{11}$$

where Q is a constant, v_i are the molar diffusion volume, M_i the molar mass of species i, p, pressure in and T, temperature.

As the transport of gas occurred through a porous structure, a Bruggeman correlation [10] was used:

$$\mathrm{D}_{ij}^{eff} = \mathrm{D}_{ij} \varepsilon^{1.5} \tag{12}$$

where D_{ij}^{eff} is the effective Stefan–Maxwell diffusivity and ε is the porosity or void fraction.

Darcy's law was used to model convection within the porous media, relating the velocity vector with the pressure gradient, the fluid viscosity and the structure permeability:

$$u = \frac{-k}{\mu_\beta} \nabla p \tag{13}$$

where k is the permeability of the porous media, and μ_β is the pore-fluid viscosity in electrode β.

Darcy's and the Stefan–Maxwell equations are coupled via the velocity vector u and density ρ. The density was calculated from:

$$\rho = \frac{\sum M_i w_i}{RT} p. \tag{14}$$

The viscosity of the anode gas μ_A is given by [30]

$$\mu_A = 1.378 \times 10^{-5} (T/298)^{1.02}. \tag{15}$$

The viscosity of the cathode gas μ_C is given by [30]

$$\mu_C = 1.094 \times 10^{-5} (T/298)^{1.02}. \tag{16}$$

4.3 Kinetics

The Butler–Volmer equation was used to describe kinetics at the anode and cathode:

$$j_V^{\beta} = S_{A\_\beta} * j_{o\_\beta} * \left((c_{\mathrm{ox}}/c_{\mathrm{ox,ref}})^{\gamma_{\mathrm{ox}}\_\beta} * \exp\left(\frac{\alpha_{an\_\beta} F}{RT}(\eta)\right) - (c_{\mathrm{red}}/c_{\mathrm{red,ref}})^{\gamma_{\mathrm{red}}\_\beta} \exp\left(\frac{-\alpha_{ct\_\beta} F}{RT}(\eta)\right)\right), \tag{17}$$

where the subscript β is either a for anode or c for cathode, S_{A_β} is the surface area, j_{o_β} the exchange current density at electrode β, $(c_{\mathrm{ox}}/c_{\mathrm{ox,ref}})$ and $(c_{\mathrm{red}}/c_{\mathrm{red,ref}})$ are the concentration ratios of the oxidised and reduced chemical states, respectively.

In hydrogen fuel cells, the activity of the anode is typically far greater than that of the cathode. Since the anode is not the performance limiting electrode, the value for j_o is not critical to the accuracy of the model, unless very low partial pressures of gases are experienced. The exchange current density, 5.7×10^4 A m^{-2}, used in the model, was obtained from the literature [31].

In the model, kinetic data for oxygen reduction in orthophosphoric acid were used, as the PBI membrane system is doped with phosphoric acid at relatively high concentrations. The oxygen reduction exchange current densities were for oxidised platinum in 85% orthophosphoric acid [32]; their variation with temperature can be described by an Arrhenius plot of log [j_o] versus 1/T as shown in Fig. 5. The j_o values obtained from the literature were for lower temperature than used in the experimental PBI fuel cell. Therefore, the Arrhenius plot was extrapolated to obtain j_o values in the required 120–200 °C temperature range. The j_o values were measured with pure oxygen on a flat platinum surface.

In the model, the specific surface area of the catalysts was determined from

$$S_{A\_\beta} = \frac{A_{\mathrm{act}}}{V_{\mathrm{cat}}} \tag{18}$$

where A_{act} is the active area of catalyst particles, and V_{cat} is the volume of the catalyst layer.

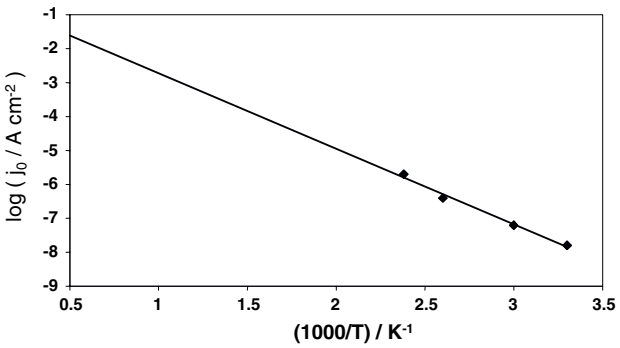

Fig. 5 Arrhenius plot of the variation of oxygen reduction exchange current density with inverse temperature for oxidised platinum in 85% orthophosphoric acid. Data (◆) taken from Huang [31]

The active area was determined from the catalyst loading, L and the platinum surface area, R_{Pt} which depends on the platinum to carbon ratio [33]. Thus, the surface area and specific surface area are given by:

$$A_{\mathrm{act}} = LabR_{\mathrm{Pt}}. \tag{19}$$

$$S_{A\_\beta} = \frac{LR_{\mathrm{Pt}}}{c}, \tag{20}$$

where a and b, are the cross section dimensions of the MEA and c, is the catalyst layer thickness.

The loading, Pt/C carbon ratio and width give an indication of the pore size within the catalyst layer.

4.4 Electrical resistance

4.4.1 Electronic resistance

In the fuel cell, there are three regions containing carbon materials; catalyst layer, microporous layer and diffusion layer. Ohm's law was used to estimate voltage losses in these components:

$$j_e = \sigma_{eff} \nabla \phi_e \tag{21}$$

where σ_{eff} is the effective conductivity for each material.

4.4.2 Ionic resistance

In the catalysts layers the potential drop due to ionic resistance is estimated from:

$$j_i = \kappa_{eff} \nabla \phi_i \tag{22}$$

where κ_{eff} is the effective conductivity for each catalyst layer.

In the model, the effect of humidity on the conductivity of the PBI membrane was included. The humidity was calculated using the ratio of partial pressure to saturation pressure:

$$\text{Hum} = \frac{p_{\text{H}_2\text{O}}}{p_{\text{sat}}(T)} * 100\% \tag{23}$$

where, Hum is the humidity of the water, $p_{\text{H}_2\text{O}}$ is the partial pressure of water at the membrane|cathode catalyst layer and p_{sat} (T) is the saturation pressure.

A temperature function for the saturation pressure p_{sat} (T) was constructed using published data [34]. The saturation pressure varied from 1 bar at 100 °C to 9 bar at 175 °C.

An Arrhenius equation was used to describe the relationship between conductivity, temperature and humidity [8]:

$$\kappa = \frac{\kappa_o}{T}\exp\left(\frac{-E_a}{RT}\right) \tag{24}$$

using two functions of humidity

$$\begin{aligned} f_1(\text{Hum}) &= E_a \\ f_2(\text{Hum}) &= \kappa_o \end{aligned}. \tag{25}$$

The humidity was calculated using a model of water cross over as follows.

4.5 Water transport

The water balance in the PBI membrane fuel cell is an important factor that can determine its performance. The transport of water from the anode (present in the hydrogen feed stream) to the cathode or from cathode to anode was included in the model. The degree of humidification of anode and cathode, and the water production at the cathode, determine the direction of water crossover; from anode to cathode or vice versa. The model uses the Stefan–Maxwell equations for the water flux in the anode and cathode.

In the case of water transport through the membrane, the flux was described by Fick's Law:

$$J_{\text{H}_2\text{O}} = -\hat{D}_{\text{H}_2\text{O}}\nabla c_{\text{H}_2\text{O}} \tag{26}$$

where $\hat{D}_{\text{H}_2\text{O}}$ is the diffusion coefficient of water vapour in the phosphoric acid loaded membrane.

Water is assumed to be in the vapour phase. However, in future work the interaction of water vapour absorbed into the liquid acid will be examined.

The boundary conditions on the anode|membrane and the membrane|cathode were:

$$\text{Fick's Diffusion Flux} = \text{Stefan} - \text{Maxwell Diffusion Flux}$$

$$J_{\text{H}_2\text{O}} = N_{\text{H}_2\text{O}} \tag{27}$$

$$\text{Stefan} - \text{Maxwell Diffusion Flux} = \text{Fick's concentration}$$

$$\frac{px_{\text{H}_2\text{O}}}{RT} = c_{\text{H}_2\text{O}}. \tag{28}$$

In the membrane model, it was assumed that there was zero flux of carbon dioxide, hydrogen, oxygen and nitrogen. However, in future work, the permeabilities of hydrogen and oxygen and their cross over effects on open circuit potentials will be considered.

4.6 Solution technique

The equations for the fuel cell model are given in the Appendix. The model equations were solved using Comsol Multiphysics, which is a PDE solver, implementing the Finite Element Method. Formerly an extension of MATLAB, COMSOL Multiphysics has developed into its own independent platform based on C and has been used previously to model fuel cells [15–17]. The parametric non-linear solver was used in a potential range of 0.1 V up to the open circuit voltage with an incremental value of 0.1 V. Since many of the equations were coupled, the problem was highly non-linear. To obtain convergence, the source terms $(\bar{R})$ were started at 0, then solved and then the source term increased and the solution resolved. This procedure was continued until the required source value was reached and solved. This technique helps the solution converge, whilst other Multiphysic's facilities, such as the re-meshing, were utilised to help obtain an accurate solution.

The values of parameters used in the model are given in Table 2.

5 Results and discussion

5.1 Fuel cell performance

Preliminary experiments were carried out in a fuel cell at temperatures between 125 and 200 °C, with electrodes prepared by both ink preparation methods. As expected, an increase of temperature improved the cell performance because of the improved conductivity of the membrane and the higher activity of the electrocatalysts.

Figure 6 shows the cell performance for a temperature of 150 °C. In general, electrode A gave a slightly superior performance; i.e. higher currents at fixed potential, than

Table 2 Physical property parameters

Parameters	Description	Units	Values
W_A_D	Anode diffusion width	μm	205
W_A_M	Anode micro porous width	μm	40
W_A_R	Anode catalyst width	μm	30
W_M	Membrane	μm	50
W_C_R	Cathode catalyst layer width	μm	20
W_C_M	Cathode diffusion layer width	μm	205
W_C_D	Cathode micro porous layer width	μm	40
j_{o_a}	Anode exchange current density (function of temperature)	A m^{-2}	10^5
j_{o_c}	Cathode exchange current density (function of temperature)	A m^{-2}	$\log(i_o) = 2.2266 * 1000/T - 0.4959$
σ_{AD}	Anode diffusion layer electron conductivity	S m^{-1}	100
σ_{AM}	Anode micro porous layer electron conductivity	S m^{-1}	100
σ_{AC}	Anode catalyst layer electron conductivity	S m^{-1}	100
σ_{CD}	Cathode diffusion layer electron conductivity	S m^{-1}	100
σ_{CM}	Cathode micro porous layer electron conductivity	S m^{-1}	100
σ_{CC}	Cathode catalyst layer electron conductivity	S m^{-1}	100
κ_{IA}	Anode catalyst layer Ion conductivity	S m^{-1}	$\kappa_{IM}e^{1.5}$
κ_{IM}	Membrane layer ion conductivity	S m^{-1}	2–4 (varying with temp)
κ_{IC}	Cathode catalyst layer ion conductivity	S m^{-1}	$\kappa_{IM}e^{1.5}$
ε_{AD}	Anode diffusion layer porosity	No units	0.4
ε_{AM}	Anode micro porous layer porosity	No units	0.2
ε_{AC}	Anode catalyst layer porosity	No units	0.1
ε_{CD}	Cathode diffusion layer porosity	No units	0.4
ε_{CM}	Cathode micro porous layer porosity	No units	0.2
ε_{CC}	Cathode catalyst layer porosity	No units	0.1
K_{AD}	Anode diffusion layer permeability	M^2	$1.5938\ 10^{-11}$
K_{AM}	Anode micro porous layer permeability	M^2	$(3/4)\ (1.5938 \times 10^{-11})$
K_{AC}	Anode catalyst layer permeability	M^2	$(1/2)\ (1.5938 \times 10^{-11})$
K_{CD}	Cathode diffusion layer permeability	M^2	1.5938×10^{-11}
K_{CM}	Cathode micro porous layer permeability	M^2	$(3/4)\ (1.5938 \times 10^{-11}$
K_{CC}	Cathode catalyst layer permeability	M^2	$(1/2)\ (1.5938 \times 10^{-11})$

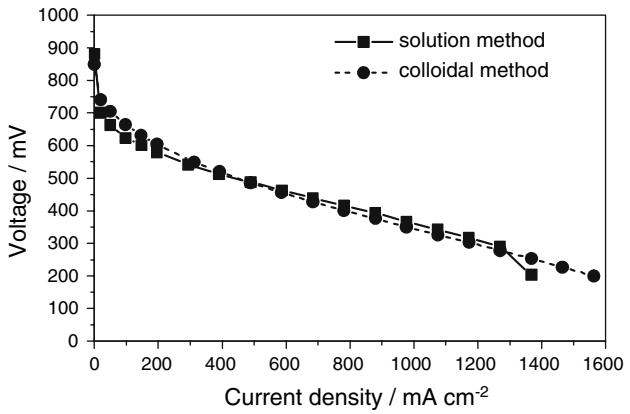

Fig. 6 Cell polarisation data for colloidal and solution electrodes at 150 °C in oxygen gas (atmospheric pressure). ■: solution electrode B. ●: colloidal electrode A

electrode B due to its more open structure and the greater surface area of the catalyst, as measured by cyclic voltammetry. It can be seen that the performance of electrode A was superior to that of electrode B at low current densities. This result was due to its, superior oxygen reduction performance and greater catalytic surface area, as measured by cyclic voltammetry. At higher current densities, electrode A also gave a superior performance to that of electrode B, since the large pore size of the electrode helped diffusion of reactants towards the catalyst sites.

Figure 7 shows the cell performance at three temperatures of operation; 125, 150 and 175 °C. The cell performance improved with an increase in temperature and at 175 °C gave a peak power density of 500 mW cm^{-2} and a current density of 750 mA cm^{-2} at a cell voltage of

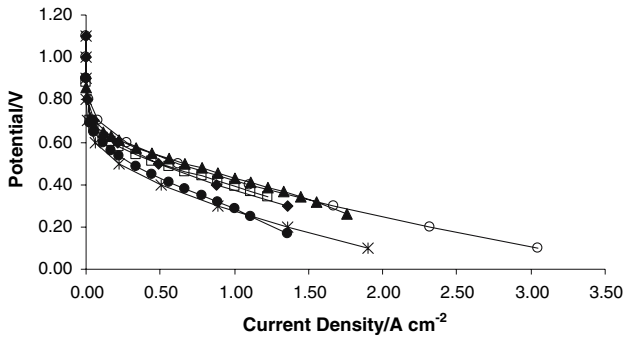

Fig. 7 Comparison of model and experimental fuel cell polarisation curves. Pt loading/0.5 mg cm^{-2}, Pt/C ratio 50%, width 20 μm, pressure 1 bar, oxygen (atmospheric pressure). Temperature: (A) ● 125 °C, (B) □ 150 °C, (C) ▲ 175 °C. Model results at temperature: (D) ⚹ 125 °C, (E) ◆ 150 °C, (F) ◯ 175 °C

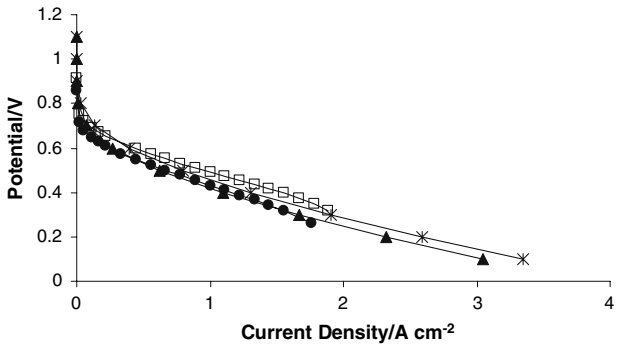

Fig. 8 The effect of pressure on fuel cell performance. Comparison of model and experiment. Pt loading/0.5 mg cm^{-2}, Pt/C ratio 50%, width 20 μm, Temperature 175 °C, and 2% humidification. Oxygen gas. (A) ● Experimental pressure 1 bar (atmospheric pressure), (B) □ Experimental pressure 2 bar, (C) ▲ Model pressure 1 bar, (D) ⚹ Model pressure 2 bar

0.5 V. The effect of gas pressure on the cell performance is shown in Fig. 8. Increasing the pressure from 0 to 1.0 bar (gauge) increased the peak power density from 485 to 630 mW cm^{-2} at 175 °C.

5.2 Model validation

Figures 7 and 8 compare the experimental results and simulated results of the model, for the PBI fuel cell at different pressures and cell temperatures. The electrocatalyst loading used in the model and experiment was 0.5 mg cm^{-2}. With a 50% Pt/C ratio, this gave a surface area of platinum of 88 m^2 mg^{-1} [8]. The cathode catalyst thickness was 50 μm and the anode catalyst width was 30 μm. These widths were obtained experimentally from scanning electron microscopy (SEM) of the cross section of the MEA.

As expected, the simulated fuel cell performance improved with increasing temperature and pressure, in agreement with experiment. Cell current densities of 1 A cm^{-2} were achieved at cell voltages of 0.4–0.5 V, at the higher temperatures, realising power densities of up to 500 mW cm^{-2}. In experiments, the open circuit potentials, typically in the range of 0.8–0.9 V depending upon operating conditions, were lower than predicted thermodynamically (Fig. 4). The low values of open circuit potentials were due to several factors, including cross over of hydrogen from anode to cathode and oxygen from cathode to anode, which created mixed potentials. In addition, coverage of platinum electro-catalyst surfaces with oxides and impurities would have affected their equilibrium potential.

In the model, the exchange current density for oxygen reduction on Pt with PBI/H_3PO_4, was considered to have a value between those reported for phosphoric acid and Nafion®. The j_0 value for oxygen is given in Table 2 using the Arrhenius relationship calculated from Fig. 5. The value used is in general agreement with estimated values from in-situ measurements of exchange current densities for oxygen reduction in operating fuel cells.

Figure 8 shows a comparison of experimental and simulated data at two different operating pressures. Not surprisingly, an increase in pressure improved the cell performance. The PBI fuel cell model simulations were in reasonable agreement with experimental data and there was good agreement in the kinetic region of the fuel cell characteristic voltage/current density curve. Overall the model gave acceptable predictions of the effect of pressure and temperature on fuel cell polarisation.

Although the model was able to predict the fuel cell performance satisfactorily, there were a number of aspects that can be improved. It would aid the model if values of the equilibrium potential allowed for the effects of fuel and oxidant crossover and also accommodated the influence of PBI covering all or part of the catalyst layers. In addition, the effect of hydrogen and oxygen crossover on kinetics, by estimating the mixed potentials at cathode and anode using suitable mechanistic models of oxygen reduction and hydrogen oxidation, coupled with appropriate transport of gases through the membrane should be considered. The effect of varying proton concentration and water activity, and oxygen and hydrogen solubility in the catalyst layers can also be considered. In this way, the model could be extended to consider oxygen solubility and transport through a "thin film" of PBI polymer covering and connecting the electrocatalyst particles.

Furthermore, in the fuel cell, the interaction between the water and the acid can be complicated. At lower temperatures, the orthophosphoric acid concentration may be lower than 85%, when the water content is greater, and so the j_o value may also be lower to account for this.

In the experiments and model, the quantities of water vapour produced were relatively small; typical exit partial pressures in the cathode exhaust gas were a maximum of 0.25 bar. In the experiments, hydrogen was supplied as a pure gas stream. However, future experiments will use reformate gas produced from methanol steam reforming. The presence of water vapour and carbon dioxide (and CO at lower temperatures) is thus likely to have an impact on cell performance. In particular, this would influence the behaviour of the cathode, through a lower oxygen partial pressure, and the anode, through CO adsorption.

5.3 Effect of water vapour

Figure 9 shows the change in oxygen partial pressure through the cathode catalyst layer for a temperature of 175 °C. As expected, the partial pressure decreased close to the membrane due to the higher local current densities. The partial pressures of oxygen also decreased with increasing cell voltage, due to the greater consumption of oxygen at the resulting higher current densities. However, the changes in partial pressure were relatively small due to the excess of air used in the experiments.

5.4 Partial pressure, potential and current distributions

One of the features of the fuel cell model was that it incorporated the inherent variation in reactant pressures and potential distributions that arise in the catalyst regions

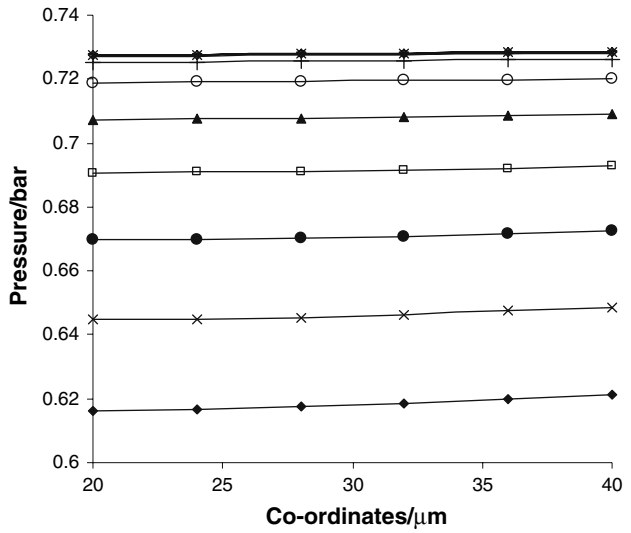

Fig. 9 Variation of the partial pressure of oxygen in the cathode catalyst layer. $\phi_e = U_{cell}$—valid on $C_F|C_D$ boundary, see "Table 1 Governing equations". U_{cell}: ◆ 0.1 V, × 0.2 V, ● 0.3 V, □ 0.4 V, ▲ 0.5 V, ◯ 0.6, | 0.7 V, — 0.8 V, – 0.9 V, ◇ 1.0 V, ⚹ 1 V

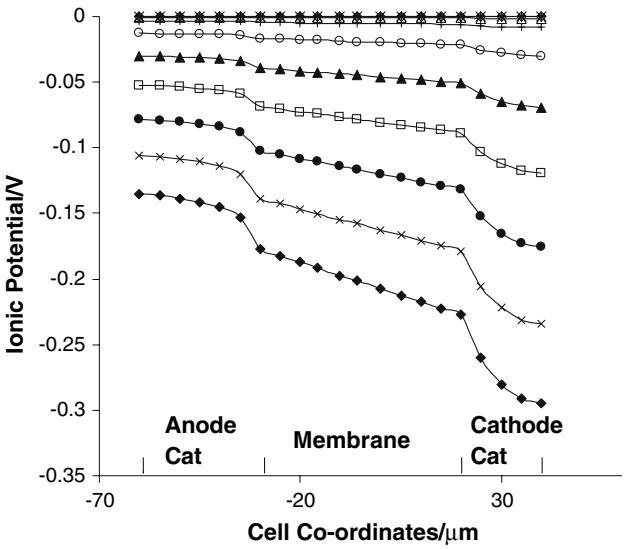

Fig. 10 Ionic potential distribution through the anode catalyst layer, membrane and cathode catalyst layer. $\phi_e = U_{cell}$—valid on $C_F|C_D$ boundary, see "Table 1 Governing equations". U_{cell}: ◆ 0.1 V, × 0.2 V, ● 0.3 V, □ 0.4, ▲ 0.5 V, ◯ 0.6 V, | 0.7 V, △ 0.8 V, – 0.9 V, ◇ 1.0 V, ⚹ 1.1 V

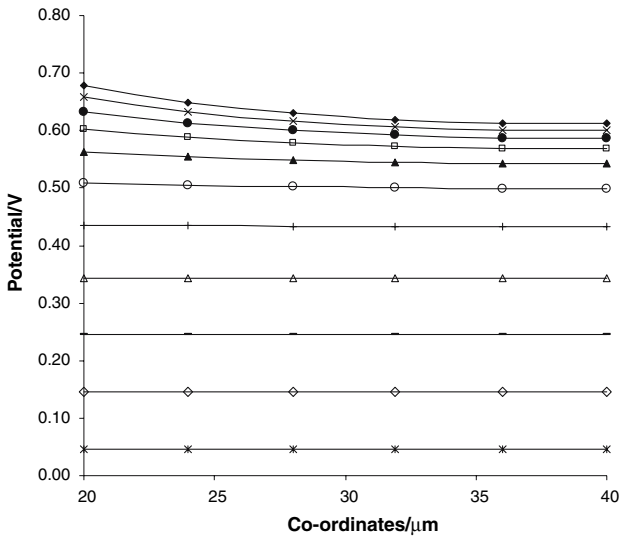

Fig. 11 Predicted overpotential distribution through the cathode catalyst layer. $\phi_e = U_{cell}$—valid on $C_F|C_D$ boundary, see "Table 1 Governing equations". U_{cell}: ◆ 0.1 V, × 0.2 V, ● 0.3 V, □ 0.4, ▲ 0.5 V, ◯ 0.6 V, | 0.7 V, △ 0.8 V, – 0.9 V, ◇ 1.0 V, ⚹ 1.1 V

and gas diffusion regions. Figures 10, 11 show typical variations in electrode potentials in the cathode catalyst region (conditions as Fig. 5 case c, 175 °C). As expected, higher cell voltages caused greater potential drops in the structures due to the greater current densities attained. A typical variation in current density in the cathode catalyst region is shown in Fig. 12, for condition c) 175 °C in Fig. 5. The variations in current density became greater at

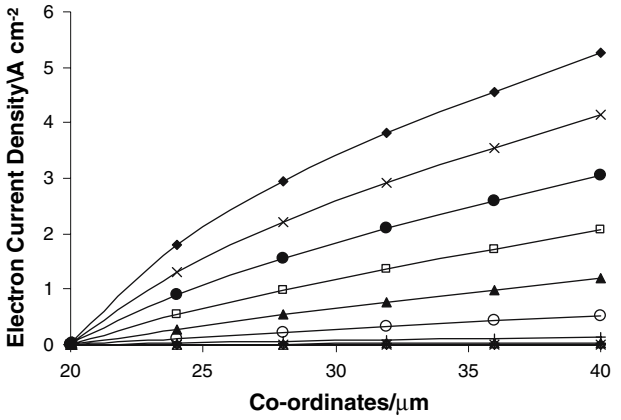

Fig. 12 Electronic current distribution in the cathode catalyst layer. U_{cell}: ◆ 0.1 V, × 0.2 V, ● 0.3 V, □ 0.4, ▲ 0.5 V, ◯ 0.6 V, | 0.7 V, △ 0.8 V, – 0.9 V, ◇ 1.0 V, ✳ 1.1 V

higher cell voltages and demonstrated the higher electrocatalyst activity in the region close to the membrane.

5.5 Effects of fuel cell parameters

5.5.1 Pt loading

The effects of varying the cathode platinum loadings were considered, to enable some degree of optimisation of the platinum used in the cathode. Figure 13 shows that, as expected, predicted fuel cell performance improved with increasing cathode catalyst loading and was acceptable even with a catalyst loading as low as 0.05 mg cm^{-2}. However, when the power density was normalised by the platinum loading, the data in Fig. 13 predicts greater power density per unit mass of catalyst (W cm^{-2} (g Pt)$^{-1}$) at lower platinum loading.

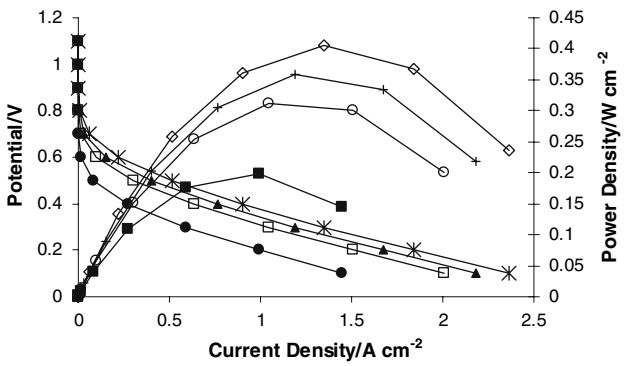

Fig. 13 Effect of catalyst loading on cell polarisation and power densities. Atmospheric pressure, temperature 125 °C, anode loading 0.5 mg cm^{-2}, cathode Pt/C ratio 30%. Cell polarisation: Pt loading/mg cm^{-2}—● 0.05, □ 0.5, ▲ 1.0, ✳ 2.0. Power densities: Pt loading/mg cm^{-2}—■ 0.05, ◯ 0.5, + 1.0, ◇ 2.0

5.5.2 PBI loading

In fuel cell catalyst layers, the introduction of PBI as an ionic bridge between the Pt catalysts is an important factor in achieving acceptable fuel cell performance. The ionic and electron conductivities in the catalyst layer were influenced by the volume fractions of PBI and catalyst in the layer. Since the ionic conductivity was an order of magnitude lower than the electronic conductivity, this factor is more critical to the accuracy of the model. The volume fraction of each material in the catalyst layer was calculated from the weight (W) and the density, ρ, of the materials in 1 cm^2 of that layer, the weight being calculated from the loading per cm^2.

For each case, the same platinum loading was considered, although the carbon loading (Vulcan XC-72) was varied. To maintain a constant volume fraction of e_{pbi} = 0.09, the volume of PBI, V_{pbi}, was varied and hence so was the weight W of PBI added. When calculating the volume fraction, the pore size and phosphoric acid were considered to make a negligible contribution.

$$\text{Volume fraction of PBI}, e_{pbi} = \frac{V_{pbi}}{(V_{pbi} + V_{pt} + V_{cb})} = 0.09$$

The densities used to calculate the surface area and electrode width were: 1.3, 21.45 and 0.27 g cm^{-3} for PBI, platinum and Vulcan XC-72, respectively. The values of electrode width and surface area used in the simulations are given in Table 3. In the simulation, Bruggeman's correlation was used to calculate the catalyst ionic conductivity [35]:

$$\kappa_{IA} = \kappa_{IM} e_{pbi}^{1.5} \text{ and } \kappa_{IC} = \kappa_{IM} e_{pbi}^{1.5}$$

Figure 14 shows the effect of catalyst loading on cell voltages and power densities, the highest peak power density being achieved with the electrocatalyst of 40 wt.% Pt. Up to a current density of ca. 0.8 A cm^{-2}, the catalyst with 60 wt.% Pt gave the lowest cell voltage and the catalyst of 20 wt.% Pt gave, marginally, the highest voltage, because of its having the highest overall electrochemically active surface area. At higher current densities, mass transport and electrical resistance effects counteracted the kinetics effects, due to the thicker catalyst layer with the lower wt.% of Pt/C, thus leading to lower performance. Therefore, there was an optimal wt.% catalyst which maximises power density. Of course this optimum was at the expense of reduced fuel efficiency, due to the relative low voltage. Thus, the model provided a means of predicting optimal catalyst loadings and electrode layer compositions for a particular set of operating conditions.

Table 3 Surface area and electrode widths for different catalyst wt%

	W (mg cm^{-2})	V/10^{-11}m^3	Width (μm)	Surface area/10^7 m^{-1}
10% Pt/C			Total 168	0.4
PBI	2.1	16.5	1.6	
Carbon Vulcan XC-72	4.5	1670	167	
20% Pt/C			Total 81	0.8
PBI	0.95	73.5	7.35	
Carbon Vulcan XC-72	2	741	74.1	
30% Pt/C			Total 47	1.2
PBI	0.55	42.3	4.2	
Carbon Vulcan XC-72	1.17	432	43	
40% Pt/C			Total 30	1.67
PBI	0.36	27.7	2.7	
Carbon Vulcan XC-72	0.75	277	27.7	
50% Pt/C			Total 20	2.2
PBI	0.24	1.85	1.8	
Carbon Vulcan XC-72	0.5	185	18.5	
60% Pt/C			Total 13.5	2.7
PBI	0.16	12.5	1.25	
Carbon Vulcan XC-72	0.33	123	12.3	
For every case				
Platinum	0.5	2.3	0.23	

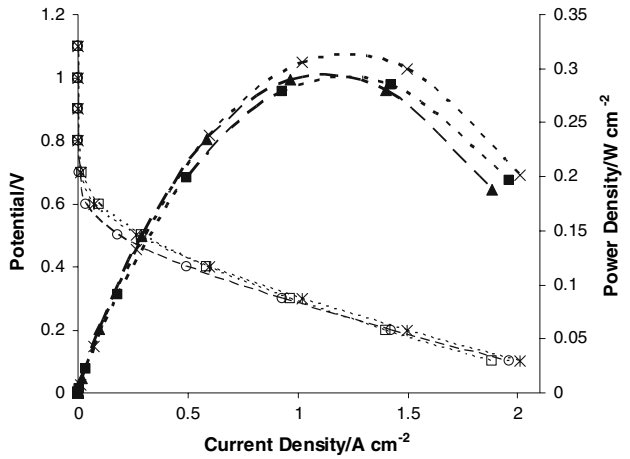

Fig. 14 Effect of Pt/C ratio on fuel cell performance with constant ε_{PBI}. Cell polarisation: Pt/C ratio/%—□ 20, ⨯ 40, ○ 60. Power densities: Pt/C ratio/%—▲ 20, × 40, ■ 60

6 Conclusions

A model of a high temperature fuel cell using PBI membranes has been developed using transport and kinetic equations. The model accounts for one dimensional electrode potential and reactant partial pressure distributions in the structure, enabling predictions of the effects of cell temperature, pressure and gas compositions, on voltages and power densities. Good agreement with experimental data was obtained within the limitations of using published, kinetic data for oxygen reduction in phosphoric acid and mass transport data. The model can be potentially used to optimise electrode structure and electrocatalyst composition in the electrode layers.

Acknowledgements The authors acknowledge the support of EPSRC through award no EP/C002601; Supergen; fuel cell consortium and the associated funding supplied by Dstl to M Mamlouk. The EU also supported M Mamlouk through project number SES6-CT-2004-502782, FURIM.

Appendix: The fuel cell model governing equations

Both the anode and cathode have the same layered structure, with similar physical phenomena occurring. As a result, they share some of the same boundary conditions and equations. To avoid duplication, each row represents the anode region or boundary and the corresponding cathode region or boundary with $i = H_2$, H_2O, CO for anode regions and $i = O_2$, N_2, H_2O for cathode regions. Equations and conditions were assumed valid for both cathode and anode, unless specified otherwise.

The notation | represents a boundary between two layers. i.e. $A_F|A_D$ is the boundary between the anode flow channel and anode diffusion layer.

Valid in region or boundary	Regional equations or boundary condition $i = H_2$, H_2O, CO for A regions and $i = O_2$, N_2, H_2O for C regions
$A_F\|A_D$	$\phi_e = 0$—only valid on $A_F\|A_D$ boundary
$C_F\|C_D$	p, w_{H_2}, w_{H_2O}—all equal to a reference on $A_F\|A_D$ boundary
	$\phi_e = U_{cell}$—only valid on $C_F\|C_D$ boundary
	$p, w_{O_2}, w_{H_2}, w_{N_2}$—all equal to a reference on $C_F\|C_D$ boundary
A_D	$\nabla \cdot (-\rho w_i \sum_K D_{1K}(\nabla x_K + (x_K - w_K)\nabla p/p)) = \bar{R}$
	K is the summation of all the species
C_D	$\sum_i \omega_i = 0$
	$\nabla \cdot j_e = 0$
	$j_e = \sigma \nabla \phi_e$
	$-\nabla \cdot (\rho * \frac{k_p}{\mu_\beta} \nabla p) = 0$
	$\rho = \frac{\sum M_i w_i}{RT} p$
$A_D\|A_R$	$j_s = \kappa_{eff} \nabla \phi_s = 0$
$C_R\|C_D$	$j_e = \sigma_{eff} \nabla \phi_e$ is continuous
	ω_i continuous
A_R	$\nabla \cdot (-\rho w_i \sum_K D_{1K}(\nabla x_K + (x_K - w_K)\nabla p/p)) = \bar{R}$
	K is the summation of all the species
C_R	$\sum_i w_i = 0$
	$j_V^\beta = S * j_{o\_\beta} * \left((c_{ox}/c_{ox,ref})^{\gamma_{ox}} * \exp\left(\frac{\alpha_a F}{RT}(\eta)\right) - (c_{red}/c_{red,ref})^{\gamma_{red}} \exp\left(\frac{-\alpha_c F}{RT}(\eta)\right)\right)$ where β = A for anode or β = C for cathode
	$\bar{R} = -\left(\frac{M_{H_2}}{2} * F\right) * j_V^A$ for A_R
	$\bar{R} = -\left(\frac{M_{O_2}}{4F} - \frac{M_{H_2O}}{2F}\right) * j_V^C$ for C_R
	$\nabla \cdot j_s = -\nabla \cdot j_e = j_V^A$ for A_R
	$\nabla \cdot j_s = -\nabla \cdot j_e = j_V^C$ for C_R
	$j_e = \sigma_{eff} \nabla \phi_e$
	$j_s = -\kappa_{eff} \nabla \phi_s$
	$-\nabla \cdot (\rho * \frac{k_p}{\mu_\beta} \nabla p) = \bar{R}$
$A_R\|M$	$j_e = \sigma_{eff} \nabla \phi_e = 0$
$M\|C_R$	$J_{H_2O} = N_{H_2O}$
	$\frac{p x_{H_2O}}{RT} = c_{H_2O}$
	$\kappa_{eff} \nabla \phi_s$ is continuous
	$\nabla \cdot (-\rho w_i \sum_K D_{1K}(\nabla x_K + (x_K - w_K)\nabla p/p)) = \bar{R}$ is insulated
	$-\nabla \cdot (\rho * \frac{k_p}{\mu_\beta} \nabla p) = 0$
M	$\kappa_{eff} \nabla \phi_s$ is continuous

References

1. Savinell R, Yeager E, Tryk D, Landau U (1994) J Electrochem Soc 141:L46
2. Alberti G, Casciola M, Massinelli L, Bauer B (2001) J Membrane Sci 185:73
3. Yang C, Costamagna P, Srinivasan S, Benziger J, Bocarsly AB (2001) J Power Sources 103:1
4. Costamagna P, Yang C, Bocarsly AB, Srinivasan S (2002) Electrochim Acta 47:1023
5. Mehta V, Cooper JS (2003) J Power Sources 114:32
6. Kawahara M, Morita J, Rikukawa M, Sanui K, Ogata N (2000) Electrochim Acta 45:1395
7. Li Q, He R, Jensen JO, Bjerrum NJ (2004) Fuel Cells 4:147
8. Ma YL, Wainright JS, Litt MH, Savinell RF (2004) J Electrochem Soc 151:A8–A16
9. Asensio JA, Borros S, Gomez-Romero P (2004) J Electrochem Soc 151:A304
10. Bernardi DM, Verbugge MW (1992) J Electrochem Soc 139:2477
11. Mazumder S, Cole JV (2003) J Electrochem Soc 150:A1503
12. Mazumder S, Cole JV (2003) J Electrochem Soc 150:A1510
13. Hu M, Gu A, Wang M, Zhu X, Yu L (2004) Convers Manage 45:1861
14. Hu M, Zhu X, Wang M, Gu A, Yu L (2004) Convers Manage 45:1883
15. Mennola T, Noponen M, Aronniemi M, Hottinen T, Mikkola M, Himanen O, Lund P (2003) J Appl Electrochem 33:979
16. Noponen M, Birgersson E, Ihonen J, Vynnycky M, Lundblad A, Lindbergh G (2004) Fuel Cells 4:365
17. Birgersson E, Noponen M, Vynnycky M (2005) J Electrochem Soc 152:A1021
18. Guvelioglu GH, Stenger HG (2005) J Power Sources 147:95
19. Scott K, Sun YP (2004) Fuel Cells 4:30
20. Cheddie DF, Munroe NDH (2006) Energy Convers Manage 47:1490
21. Cheddie DF, Munroe NDH (2006) J Power Source 160:215
22. Linares JJ, Lobato J, Rodrigo MA, Scott K (2006) Effect of the catalytic ink preparation method on the performance of high temperature polymer electrolyte membrane fuel cells. J Power Sources 157:284
23. Vogel HA, Marvel CS (1961) J Polym Sci 50:511
24. Choe EW (1994) J App Polym Sci 53:497
25. Sandor RB, Thornburg TS (1991) Polybenzimidazole solutions, US patent 5066697
26. Li Q, He R, Berg RW, Hjuler HA, Bjerrum NJ (2004) J Solid State Ionics 168:177
27. Ma Y (2004) The fundamental studies of polybenzimidazole/phosphoric acid polymer electrolyte for fuel cells. Ph.D. Thesis, Case Western University
28. U.S. Department of Energy, Office of Fossil Energy (2004) Fuel cell handbook, 7th edn
29. Atkins PW (2002) Physical chemistry, 7th edn. Oxford University Press
30. Reid RC, Prausnitz, BE, Poling BE (1987) The properties of gases and liquids, 4th edn. McGraw-Hill
31. Gang X, Li Q, Hans Aage H, Bjerrum NJ (1995) J Electrochem Soc 142:2890
32. Huang JC, (1979) J Electrochem Soc 126:787
33. De Nora Elettrodi Network (2004) E-TEK catalogue for commercial products of nobel metal catalysts on carbon
34. Knovel (2006) Knovel steam tables based on equations published by the International association for the properties of water and steam (IAPWS)©
35. Bruggeman DAG (1935) Ann Physik 24:636